

The frequency, temperature, and magnetic field dependence of ferromagnetic resonance and anti-resonance in $\text{La}_{0.8}\text{Sr}_{0.2}\text{MnO}_3$

Andrew Schwartz,^{*} Marc Scheffler,[†] and Steven M. Anlage

*MRSEC and Center for Superconductivity Research, Department of Physics, University of Maryland
College Park, MD 20742-4111
(lsmo4.tex, October 24, 2018)*

Employing a broadband microwave reflection configuration, we have measured the complex surface impedance, $Z_S(\omega, T, H)$, of single crystal $\text{La}_{0.8}\text{Sr}_{0.2}\text{MnO}_3$, as a function of frequency (0.045–45 GHz), temperature (250–325 K), and magnetic field (0–1.9 kOe). The microwave surface impedance depends not only on the resistivity of the material, but also on the magnetic permeability, $\hat{\mu}(\omega, T, H)$, which gives rise to ferromagnetic resonance (FMR) and ferromagnetic anti-resonance (FMAR). The broadband nature of this experiment allows us to follow the FMR to low frequency and to deduce the behavior of both the local internal fields and the local magnetization in the sample.

PACS numbers: 76.50.+g, 78.70.Gq, 75.30.Vn, 76.60.Jx

I. INTRODUCTION

The recent discovery of large negative magnetoresistance in the manganite perovskites $\text{La}_{1-x}\text{A}_x\text{MnO}_3$ (where A is a divalent cation, typically Ca, Sr, or Ba) has led to numerous studies of both the physics and potential technological applications of these materials.^{1–3} A great deal of work has been done on the dc transport^{1–5} and optical^{6–8} properties of these so-called colossal magnetoresistive (CMR) oxides. But by comparison the microwave properties have not been extensively investigated, and the work that has been done has generally been limited to a few frequencies by the resonant techniques employed.^{9–13} In addition, these measurements generally do not produce quantitative values of the surface resistance or the surface reactance.

Because of the relatively high resistivities of the CMR compounds, the enhanced sensitivity of resonant microwave techniques is not necessary. In this paper we present the results of our broadband, non-resonant microwave surface impedance measurements, in which we have quantitatively determined the complex surface impedance, $Z_S(\omega, T, H) = R_S(\omega, T, H) + iX_S(\omega, T, H)$, of $\text{La}_{0.8}\text{Sr}_{0.2}\text{MnO}_3$ single crystals over three decades in frequency, and as a function of both temperature and applied external magnetic field. We previously reported measurements of the surface impedance of this material in zero applied field, and showed that it is possible to extract the temperature dependence of the spontaneous magnetization from these data.¹⁴ Here we focus on the surface impedance in an applied magnetic field, and show that the spectra can be well described by the Landau-Lifshitz-Gilbert expression for the dynamic susceptibility of a ferromagnetic system. We present quantitative analysis of the field and temperature dependence of the ferromagnetic resonance and anti-resonance features observed in the spectra, and demonstrate that it is possible to extract the local magnetization and internal fields from

these data.

$\text{La}_{0.8}\text{Sr}_{0.2}\text{MnO}_3$ (LSMO) has a ferromagnetic phase transition with a Curie temperature T_C of approximately 305.5 K.¹⁴ It is well established that the low temperature phase is a ferromagnetic metal (the resistivity drops dramatically below T_C), while above T_C the system is paramagnetic, and the resistivity exhibits a negative slope with respect to temperature. The resistivity has a maximum around $T_p = 318$ K, significantly above T_C , which is typical in these manganite materials.¹¹

II. EXPERIMENTAL SETUP

In order to measure the temperature and frequency dependence of the complex surface impedance we have terminated a coaxial transmission line with the sample and measured its complex reflection coefficient. We have reported the details of this experimental geometry elsewhere,¹⁵ and will therefore give only a brief overview of the technique here. In particular, our original implementation of the method was for the study of superconducting thin films, so we will discuss its use here on bulk single crystals.

This experiment is built around an HP8510C Vector Network Analyzer (NWA), which is continuously tunable over three decades from 45 MHz to 50 GHz. The phase-locked signal from the NWA is sent along a coaxial transmission line with a modified 1.85mm coaxial connector on the other end. This modified connector has a flat face and a spring-loaded center conductor, allowing a sample to be pressed against it, thereby terminating the transmission line. The amplitude and phase of the reflected signal are measured as the source is swept throughout the entire frequency range, and the complex reflection coefficient, $\hat{S}_{11}(\omega)$, is determined as the ratio of the reflected to incident voltages. After standard NWA calibration procedures to remove the errors due to the systematic

response of the NWA and the transmission line, the complex surface impedance of the terminating material can be calculated from the reflection coefficient as follows:

$$\hat{Z}_S(\omega) = R_S(\omega) + iX_S(\omega) = Z_0 \frac{1 + \hat{S}_{11}(\omega)}{1 - \hat{S}_{11}(\omega)}, \quad (1)$$

where $Z_0 = 377\Omega$ is the impedance of free space. As discussed, due to the phase-sensitive detection capabilities of the NWA, it is possible to extract *both* the surface resistance, R_S , and the surface reactance, X_S , and the well-defined terminated transmission line geometry allows for *quantitative* evaluation of these material parameters. In addition, while this non-resonant technique does not provide the sensitivity of microwave resonator measurements, the broadband nature allows for the study of the response across three orders of magnitude in frequency, and therefore opens a unique window to dynamical processes within the material.

By passing the coaxial line through a vacuum seal into a continuous flow cryostat, in which the sample is attached to the cold finger, we have measured the reflection coefficient as the temperature of the sample is varied. Because the temperatures of interest in this study were all above 200 K, we operated the cryostat with a flow of liquid nitrogen rather than the traditional helium, and were able to achieve temperature stability on the order of a few millikelvin at all temperatures between 200 and 325 K. This allowed us to study the temperature dependence of the surface impedance, to complement the frequency dependent data.

As mentioned above, a standard calibration procedure is employed to remove systematic errors. In general there are three sources of error for which we must correct. One of these is due to the attenuation and phase delay of the coaxial transmission line between the NWA and the sample, and is therefore temperature dependent. Part of this line is within the cryogenic environment, and thus expands or contracts as the temperature is varied. Such changes in length cause changes in the phase delay and, to a lesser extent, the attenuation of the line. To correct for this, a further calibration procedure is performed. The temperature dependence of the reflection coefficient of a flat piece of bulk copper is measured as an additional calibration standard. It is measured in the same way (at the same temperatures and frequencies) as the sample. We then assume that this copper block acts as if it were a perfect short at all temperatures¹⁶ and therefore has a known reflection coefficient $\hat{S}_{11}^{\text{Cu}} = -1 + 0i$. Thus, corrected error coefficients are determined for all frequencies and temperatures of interest and the reflection coefficient of the sample can be deduced from the measured reflection coefficient.

In addition, by using two strong permanent magnets, one placed on either side of the sample, and varying the separation between them we have been able to produce a uniform static magnetic field at the sample position which can be continuously varied from 0 to 1.9 kOe. The

faces of the magnets are much larger than the size of the sample and therefore the field is expected to be relatively homogeneous throughout the sample. With this setup, we were able to study the field dependence of the surface impedance. For all of the data shown in this paper, the field was taken to its maximum value of 1.9 kOe, sufficient to saturate the magnetization, and then the data were collected as the field was lowered to zero.

III. FERROMAGNETIC RESONANCE AND ANTI-RESONANCE

In the presence of an applied external magnetic field of the appropriate magnitude, which will be discussed below, the microwave properties of ferromagnetic materials are characterized by two distinct features which result from the dispersion of the complex magnetic permeability $\mu(\omega)$:¹⁷ ferromagnetic resonance (FMR) and ferromagnetic anti-resonance (FMAR). At the FMR frequency, ω_r , the surface resistance, $R_S(\omega_r)$ shows a maximum due to a maximum in the imaginary part of the magnetic permeability, $\mu_2(\omega)$. At the same frequency, the real part of the permeability, $\mu_1(\omega)$, has a zero-crossing with negative slope. In order to satisfy the condition $\mu_1(\omega \rightarrow \infty) = 1$, it is necessary that there be another zero-crossing, with positive slope, at a frequency $\omega_{ar} > \omega_r$. At this point, as will be shown below, the surface resistance shows a local minimum, commonly known as the ferromagnetic *anti*-resonance. This reduction in the surface resistance is due to an increase in the penetration of the fields into the material. It can also be shown that, in general, both ω_r and ω_{ar} depend not only on the externally applied field but also on the local internal magnetization of the material. Therefore, our measurements of the microwave surface impedance have yielded information about the magnetization of LSMO.

A. Dynamic Susceptibility

In order to understand the origins of the ferromagnetic resonance and anti-resonance in more detail, and to be able to analyze the broadband measurements presented here, it is necessary to examine the full functional form of the dynamic susceptibility $\chi(\omega)$.¹⁷ The starting point for the calculation of the dynamic susceptibility of a ferromagnetic material is the Landau-Lifshitz equation of motion for the magnetization vector \mathbf{M} in the presence of a magnetic field \mathbf{H} :¹⁷

$$\frac{d\mathbf{M}}{dt} = \gamma(\mathbf{M} \times \mathbf{H}) - \frac{\alpha\gamma}{M}(\mathbf{M} \times (\mathbf{M} \times \mathbf{H})), \quad (2)$$

where γ is the gyromagnetic ratio for an electron and α is a dimensionless damping parameter. The first term describes the precession of the magnetization around the applied field, and the second term describes the damping

of this precessional motion. In this form, the damping term is perpendicular to \mathbf{M} and therefore changes only the angle and not the amplitude of the magnetization vector. This expression can be simplified further by taking the cross product of \mathbf{M} with both sides. After some algebraic manipulation this gives

$$\frac{d\mathbf{M}}{dt} = \gamma^*(\mathbf{M} \times \mathbf{H}) - \frac{\alpha}{M} \left[\mathbf{M} \times \frac{d\mathbf{M}}{dt} \right], \quad (3)$$

where $\gamma^* = \gamma(1 + \alpha^2)$. In the limit of small damping ($\alpha^2 \ll 1$), $\gamma^* \approx \gamma$. This is known as the Landau-Lifshitz-Gilbert equation of motion, and α is commonly referred to as the Gilbert damping parameter.

In order to calculate the dynamic susceptibility from this equation of motion, it is necessary to choose a form for the magnetic field and thus the magnetization. In the experiment we apply a uniform static magnetic field H_0 , but the field which is important is the total *internal* magnetic field H_i , which will in general differ from H_0 , as we will discuss below. So for now we just presume that there is a total static internal field H_i oriented along the \hat{z} direction, and a microwave field $\mathbf{h}_{\text{rf},i}$, which may also differ from the applied microwave field:

$$\mathbf{H}(t) = \hat{z}H_i + \mathbf{h}_{\text{rf},i}e^{i\omega t}. \quad (4)$$

In an isotropic system, the magnetization is presumed to follow the applied field, so we assume that the static magnetization is aligned with the static field H_i and that there is a component of the magnetization with the same time dependence as the microwave field:

$$\mathbf{M}(t) = \hat{z}M_0 + \mathbf{m}_{\text{rf}}e^{i\omega t}. \quad (5)$$

By inserting Eqs. (4) and (5) into Eq. (3) we can easily calculate the susceptibility tensor $\bar{\chi}$ from the relation

$$\mathbf{m}_{\text{rf}} = \bar{\chi} \cdot \mathbf{h}_{\text{rf},i} = \begin{pmatrix} \hat{\chi}_{xx} & \hat{\chi}_{xy} & 0 \\ \hat{\chi}_{yx} & \hat{\chi}_{yy} & 0 \\ 0 & 0 & 0 \end{pmatrix} \cdot \mathbf{h}_{\text{rf},i}, \quad (6)$$

where we have assumed, as above, that the static field is in the \hat{z} direction, and that $\mathbf{h}_{\text{rf},i} \ll \mathbf{H}_i$ and $\mathbf{m}_{\text{rf}} \ll \mathbf{M}$. It is clear here that there will be no components of \mathbf{m}_{rf} along \hat{z} , and that any \hat{z} component of $\mathbf{h}_{\text{rf},i}$ will not contribute to \mathbf{m}_{rf} . This is important for the geometry we have employed, and will be discussed further below.

Before calculating the components of the susceptibility tensor, however, it is necessary to account for the fact that in general the internal fields will differ from the applied external fields due to demagnetization effects. The applied external fields will lead to a net magnetization, which in turn will produce dipoles on the surface of the sample, and these dipoles give rise to a field within the sample which opposes the applied field.¹⁷ The magnitude of such a demagnetization field (H_d) depends on the geometry of the sample and on the net magnetization. In addition, we will see later that it is necessary to allow

for the existence of small static local fields (\mathbf{H}_{loc}) within the material. Such fields might arise, for example, from anisotropy and domain structure. It is reasonable to assume that H_d will be aligned antiparallel to the applied field, but the orientation of \mathbf{H}_{loc} is likely to vary with position within the sample. However, we will also presume that it is only the component of \mathbf{H}_{loc} aligned parallel to M_0 (i.e. along \hat{z}) which will contribute to the precession of the magnetization. Thus we can write the total field within the material as follows:

$$\mathbf{H}_i = \hat{z}(H_0 - N_z M_0 + H_{\text{loc}}). \quad (7)$$

Similarly, the microwave magnetization produces a high frequency demagnetization field, so

$$\mathbf{h}_{\text{rf},i} = \mathbf{h}_{\text{rf}} - \hat{x}N'_x m_x - \hat{y}N'_y m_y, \quad (8)$$

where \mathbf{h}_{rf} is the externally applied field, and we have omitted the term $\hat{z}N'_z m_z$ because there will be no components of \mathbf{m}_{rf} along \hat{z} . N_i are the geometry-dependent demagnetization factors along the three principle axes and we have chosen to denote dynamic factors in Eq. (8) with primes because they can, in general, differ from the static factors. We will return to the precise determination of these values shortly.

Using these expressions we can write an expression for $\hat{\chi}_{xx}$, one of the nonzero diagonal components of the susceptibility tensor, as follows:

$$\hat{\chi}_{xx}(\omega) = \frac{\omega_M[(\omega_0 + i\Gamma) + N'_y \omega_M]}{\omega_r^2 - (1 + \alpha^2)\omega^2 + i\Gamma[2\omega_0 + (N'_x + N'_y)\omega_M]} \quad (9)$$

where we have introduced the linewidth $\Gamma = \alpha\omega$. Similar expressions can be obtained for $\hat{\chi}_{yy}$, and for the off-diagonal terms $\hat{\chi}_{xy}$ and $\hat{\chi}_{yx}$,¹⁸ but these will not be of importance here. In order to emphasize the dimensionless nature of the susceptibility and the fact that we have measured its frequency dependence, all of the fields have been expressed as frequencies, with the following definitions:

$$\begin{aligned} \omega_M &= \gamma^* \mu_0 M_0 \\ \omega_0 &= \gamma^* \mu_0 (H_0 - N_z M_0 + H_{\text{loc}}) \\ \omega_r &= \sqrt{(\omega_0 + N'_x \omega_M)(\omega_0 + N'_y \omega_M)}. \end{aligned}$$

It is clear from Eq. (9) that for small damping ($\alpha^2 \ll 1$), the quantity ω_r is the ferromagnetic resonance frequency. As written, these expressions are in SI units, with H_0 and M_0 in amperes-per-meter, all frequencies expressed in gigahertz, and the gyromagnetic ratio for the electron given by $\gamma/2\pi = 28 \text{ GHz/T}$.

In order to determine the form of the susceptibility it is only necessary to know the values of the demagnetization factors N_i for the geometry of interest. For an arbitrarily-shaped sample, this is a difficult task, but for certain simple geometrical shapes, the demagnetization

factors are well known. The samples of $\text{La}_{0.8}\text{Sr}_{0.2}\text{MnO}_3$ which we have investigated are disks, with diameters d and thicknesses t such that generally $t \leq 0.2d$. The static field H_0 was applied in the plane of the disk, thereby defining the z -axis. We take the x -axis to also be in the plane, and the y -axis to be normal to the surface. We can simplify the problem somewhat by taking into account the fact that the dynamic demagnetization factors (N'_x and N'_y) may be independent of the static one (N_z). In other words, the microwave fields penetrate only a short distance, the skin depth δ , into the sample. For all measured frequencies, this penetration is much less than the diameter of the sample, and therefore from the point of view of h_{rf} , and therefore m_{rf} , the sample looks like a thin plate, allowing us to set $N'_x = 0$ and $N'_y = 1$. On the other hand, the static magnetic field penetrates throughout the sample, and therefore we cannot use this argument to determine N_z . However, in Sec. IV we will show that we are able to extract a value of N_z directly from the microwave measurements.

As discussed above, the dynamic permeability, $\hat{\mu} = \mu_0(1 + \hat{\chi})$, has two distinct features: a resonance (FMR) at which μ_2 is a maximum, and a zero-crossing of μ_1 at higher frequency (FMAR). The frequencies of these two features are determined by the magnitudes of the total internal field H_i and the local magnetization M_0 , and by the demagnetization factors. With the applied field parallel to the plane of the sample, as in the measurements presented here, the FMR and FMAR frequencies are given by

$$\omega_r = \gamma^* \mu_0 \sqrt{H_i(H_i + M_0)} \quad (10)$$

$$\omega_{ar} = \gamma^* \mu_0 (H_i + M_0) \quad (11)$$

where once again we have taken $N'_x = 0$ and $N'_y = 1$. It is clear from Eqs. (10) and (11) that if we measure ω_r and ω_{ar} then we can uniquely determine both M_0 and H_i . It is worth noting that unlike in a typical magnetization measurement, this magnetization M_0 is not the net magnetization of the sample but instead is the average magnitude of the local magnetization. Thus we see that by measuring the dynamic susceptibility it is possible to extract information about the *local* magnetization of the material. Such analysis will be discussed further in Sec. IV.

B. Surface Impedance

In fact, as outlined above, the microwave reflection measurement which we have employed directly yields the surface impedance instead of the susceptibility, however the two are related through the permeability, $\hat{\mu}(\omega) = \mu_1(\omega) - i\mu_2(\omega) = \mu_0[1 + \hat{\chi}(\omega)]$, as follows:

$$\hat{Z}_S(\omega) = R_S(\omega) + iX_S(\omega) = \sqrt{i\omega\hat{\mu}(\omega)\rho_{dc}}, \quad (12)$$

where ρ_{dc} is the *dc* resistivity of the material. We have assumed that at microwave frequencies $\text{La}_{0.8}\text{Sr}_{0.2}\text{MnO}_3$

is in the Hagen-Rubens limit (i.e. $\rho_2(\omega) \ll \rho_1(\omega) \approx \rho_{dc}$), allowing us to insert a real frequency-independent value for ρ . Then we can substitute the expression for the susceptibility from Eq. (9) into Eq. (12) in order to model the complete frequency dependence of R_S and X_S and, in particular, the behavior in the vicinity of ω_r and ω_{ar} . At the ferromagnetic resonance, R_S is maximum and X_S has an inflection point with negative slope, whereas at the anti-resonance, R_S has a local minimum, while X_S has another inflection point with positive slope.

In Sec. IV we will show that with a few small modifications to account for specifics of the measurement, Eq. (12) gives an excellent description of the measured data. From such fits it is therefore possible to extract values of the local magnetization M_0 as a function of both temperature and applied magnetic field.

IV. EXPERIMENTAL RESULTS AND ANALYSIS

Employing the configuration presented in Sec. II we have measured both the surface resistance and surface reactance of $\text{La}_{0.8}\text{Sr}_{0.2}\text{MnO}_3$ as functions of frequency, temperature, and applied magnetic field. We have measured the frequency dependence from 45 MHz to 45 GHz but, as we will see, for the temperatures, magnetizations, and fields of interest in this paper the resonant features occur below 20 GHz, and we will therefore limit the discussion to that part of the frequency range. We have measured the temperature dependence of the response in the range 250–325 K, through the ferromagnetic transition at 305.5 K, and for fields of 0–1.9 kOe.

The single crystals of $\text{La}_{0.8}\text{Sr}_{0.2}\text{MnO}_3$ used in this study were grown by the floating-zone technique¹⁹ and the stoichiometry and structural integrity have been checked by x-ray diffraction and energy dispersive x-ray analysis. From a 4 mm diameter rod, we cut disk-shaped samples with thicknesses from 0.5–1 mm, and polished the surfaces to 1 μm flatness. Resistivity, ac susceptibility, and dc magnetization measurements have been reported earlier on samples cut from the same boule.¹¹

A. Surface Impedance

Figure 1 is a representative example of the data obtained, showing a surface and contour plot of $R_S(\omega, H_0)$ at $T = 301.5$ K, a few degrees below $T_C = 305.5$ K. As mentioned above, the field H_0 was applied in the plane of the disk-shaped sample. The sharp peak is the FMR absorption, which grows in intensity and moves to higher frequency as the field is increased. This is as we would expect from Eq. (10). At somewhat higher frequencies, the FMAR minimum is evident, and it also is seen to rise in frequency with increasing field, as predicted by Eq. (11).

Fixed-field cuts through the $R_S(\omega, H_0)$ data shown in Fig. 1 are displayed in Fig. 2(a); the corresponding $X_S(\omega)$ spectra are seen in Fig. 2(b). It is clear from the latter that the signature of the ferromagnetic resonance is a steep drop of $X_S(\omega)$, with maximum slope at the resonance frequency. At the anti-resonance there is a less pronounced but clearly visible rise of X_S . Both of these features are predicted by the model presented in Sec. III. From the measured resonance and anti-resonance frequencies, $\omega_r/2\pi = 6.9$ GHz and $\omega_{ar}/2\pi = 11.3$ GHz, at an applied field of $\mu_0 H_0 = 0.19$ T, we have uniquely determined the value of M_0 from Eqs. (10) and (11) as follows:

$$\mu_0 M_0 = \frac{1}{\gamma \omega_{ar}} (\omega_{ar}^2 - \omega_r^2) \quad (13)$$

where we have assumed that $\alpha^2 \ll 1$ and therefore $\gamma^* \approx \gamma$. In addition, as will be shown later, at this large applied field value $H_{loc} \ll H_0 - N_z M_0$, and therefore we can also solve Eqs. (10) and (11) for the static demagnetization factor:

$$N_z = \frac{\mu_0 H_0 \gamma \omega_{ar} - \omega_r^2}{\omega_{ar}^2 - \omega_r^2}, \quad (14)$$

With these values fixed, α and ρ_{dc} are varied to fit the $Z_S(\omega, H)$ data. The thick solid lines on Fig. 2 are fits to the $\mu_0 H_0 = 0.19$ T data with this model and the following parameters: $\mu_0 M_0 = 0.25$ T, $\alpha = 0.03$, $N'_x = 0$, $N'_y = 1$, $N_z = 0.15$, and $\rho_{dc} = 60$ m Ω -cm. The model has only been modified to account for our particular experimental geometry, in which h_{rf} is not linearly polarized, and for a small offset in R_S and slope in X_S which arise due to a contact impedance.²⁰ Similar fits can be made to the data at other temperatures and applied field values, and the model of Sec. III clearly provides an excellent description of the experimental data. The value of the damping parameter $\alpha = 0.03$ corresponds to a linewidth $\Gamma/2\pi = \alpha\omega/2\pi$ of 0.2 GHz at the FMR frequency. This translates into a 70 Oe linewidth in field space, which agrees well with the value reported earlier for this material.¹¹

The enhancement of R_S at the FMR frequency is easily understood as an enhanced absorption due to a matching of the microwave frequency to the natural precession frequency of the electronic spins within the material. The reason for the reduction of R_S at the FMAR frequency, below the value which it would have for a non-magnetic material with the same resistivity, is less obvious. However, if we presume that the microwave field is a plane wave with the spatial and temporal dependence of the electric field given by $E \propto e^{i\omega t - ky}$, then it is possible to insert this into Maxwell's equations and solve for the wavevector k . This leads, in general, to a complex wavevector given by

$$\hat{k} = \sqrt{i\omega\hat{\mu}(\omega)\sigma} = \frac{\hat{Z}_S}{\rho}, \quad (15)$$

where we have employed Eq. (12) for the second equality. As usual, the characteristic length over which the fields decay into the material, the skin depth, is given by $\delta = (Re\{\hat{k}\})^{-1}$. In a non-magnetic metal this would just be the usual $\delta = \sqrt{2/\mu_0\omega\sigma}$, but in our case it is modified by the frequency dependence of the permeability $\hat{\mu}$. Figure 3 shows the frequency dependence of this skin depth at 301.5 K and in an applied field of 0.19 T, as extracted from the data (open squares) and the model used above to fit the surface impedance data (solid line). The dashed line shows the skin depth for a non-magnetic metal with the same resistivity. What is clear in the figure is that the skin depth has a local maximum at the FMAR frequency, and is in fact enhanced over the non-magnetic value. Thus at this frequency the microwave fields penetrate farther into the sample, and the currents are flowing in this thicker layer, thereby reducing the surface resistance. However, it is worth noting that the thickness of this sample was approximately 800 μ m, and therefore it is clear that the skin depth remains smaller than the sample thickness even at the FMAR frequency.

B. Field-dependence of ω_r and ω_{ar}

From the data shown in Fig. 1 and similar data at other temperatures, we can extract the field and temperature dependence of the ferromagnetic resonance and the ferromagnetic anti-resonance frequencies. Figure 4 shows the magnetic field dependence of the ferromagnetic resonance and anti-resonance frequencies at three representative temperatures, including 301.5 K as shown in Figs. 1 and 2. As expected, both frequencies increase with increasing applied field and with decreasing temperature. As is clear from Eq. (13), the local magnetization M_0 can be directly extracted from these resonance and anti-resonance frequencies. The results of such analysis at the same three temperatures are shown in Fig. 5. As expected, once again, the magnetization is seen to grow with decreasing temperature, and also to increase slightly with applied field.

As we have mentioned above, at the higher applied fields it is possible to use Eq. (14) to determine the demagnetization factor N_z . However, we have found that it is not appropriate to apply this high-field analysis at low fields where the FMR and FMAR frequencies become independent of field (see Fig. 4). It is clear that the existence of the local fields H_{loc} cannot be neglected as the applied field approaches zero. In fact, it is precisely these fields that allowed us to observe the FMAR, and to extract the spontaneous magnetization, even in the absence of an applied field.¹⁴ In order to fully describe the data shown in Fig. 4, it is necessary to account for this field H_{loc} . We can solve Eqs. (10) and (11) for the total internal field

$$\mu_0 H_i = \frac{\omega_r^2}{\gamma \omega_{ar}}. \quad (16)$$

These data, again for the same three representative temperatures, are shown as a function of the applied field in Fig. 6.

What we see in Fig. 6 is that at 276.6 K for example, H_i is small and roughly constant for $H_0 < 0.06$ T, and then rises roughly linearly at higher fields. This can be understood in the following way. At low applied fields, there is reorientation of the magnetic domains within the sample which give rise to a demagnetization field H_d which exactly cancels H_0 . Thus in this regime $H_i = H_{loc} = 0.017$ T (because of the random orientation of H_{loc} this is an average local field throughout the sample). However, at $\mu_0 H_0 \approx 0.06$ T, the magnetic domains are all aligned, the demagnetization field saturates at $H_d = N_z M_0$, and as the external field is increased it penetrates the sample. Therefore we presume that the demagnetization field for the data at 276.6 K has the following form:

$$\begin{aligned} \mu_0 H_d &= \mu_0 H_0 & \text{for } \mu_0 H_0 \leq 0.06 \text{ T} \\ \mu_0 H_d &= N_z \mu_0 M_0 & \text{for } \mu_0 H_0 > 0.06 \text{ T.} \end{aligned} \quad (17)$$

As we have argued earlier in deriving Eq. (14), at large field values H_{loc} can be ignored. This is due in part to the fact that $H_{loc} \ll H_0$, but also to the fact that H_{loc} is randomly oriented within the sample. Therefore for fields $H_0 \gg H_{loc}$ we would expect that H_{loc} would simply broaden the FMR and FMAR lines and not shift them. If we calculate the total internal field H_i using the known applied field, the demagnetization field given by Eq. (17), and an H_{loc} which has a constant magnitude of 0.17 T but is averaged over all orientations, then we arrive at the solid line on Fig. 6. It is clear that this provides an excellent description of the dependence of the total internal field on the applied external field.

Finally, using this empirical form for H_i , and the magnetization data shown in Fig. 5, it is possible to model the complete field dependence of the ferromagnetic resonance and anti-resonance frequencies with Eqs. (10) and (11). This is shown, again only at 276.6 K, by the solid lines on Fig. 4, and it is clear that it provides an excellent description of the data throughout the entire range of applied fields. The same analysis can be carried out at other temperatures in order to obtain a full description of all of the data.

V. CONCLUSIONS

By measuring the broadband frequency dependence of the surface impedance of $\text{La}_{0.8}\text{Sr}_{0.2}\text{MnO}_3$ we have shown that the Landau-Lifshitz-Gilbert expression for the dynamic susceptibility provides an excellent description of the complete microwave spectra, including the ferromagnetic resonance and anti-resonance features. In addition, we have performed a quantitative analysis of the field dependence of these features, and have shown that they

can be modeled extremely well with rather simple expressions for the field dependence of the magnetization, the demagnetization field, and the local internal fields. To our knowledge, this is the most extensive study of the frequency, field, and temperature dependence of the microwave properties of a ferromagnet.

In addition, we would like to stress that in contrast to conventional magnetization measurements, the technique presented here is sensitive to the average *local* magnetization of the material. At each point in the sample, the local magnetization is interacting with the local static and dynamic magnetic fields to produce the dramatic FMR and FMAR features, which are then averaged over the entire sample. As we have reported earlier, this fact allowed us to measure the spontaneous magnetization of this material in the absence of any applied magnetic field.¹⁴ Conventional magnetization measurements require the application of an applied field in order to produce a net magnetization in the sample. Finally, the broadband nature of the surface impedance measurements presented here have allowed us to determine this local magnetization of $\text{La}_{0.8}\text{Sr}_{0.2}\text{MnO}_3$ over wide magnetic field and temperature ranges.

ACKNOWLEDGMENTS

We would like to thank Y. Mukovskii and colleagues at the Moscow State Steel and Alloys Institute for growing the samples used in this study. We also thank S. Bhagat and S. Lofland for providing the samples to us, and for many useful and interesting discussions about these materials. This work was supported by NSF Grant No. DMR-9624021, the University of Maryland NSF-MRSEC Grant No. DMR-0080008, and the Maryland Center for Superconductivity Research.

* Electronic address: schwartz@squid.umd.edu; Present address: Neocera Inc., 10000 Virginia Manor Rd., Beltsville, MD, 20705.

† Present address: 1. Physikalisches Institut, Universität Stuttgart, D-70550 Stuttgart, Germany.

¹ R. von Helmolt, J. Wecker, B. Holzapfel, L. Schultz, and K. Samwer, Phys. Rev. Lett **71**, 2331 (1993).

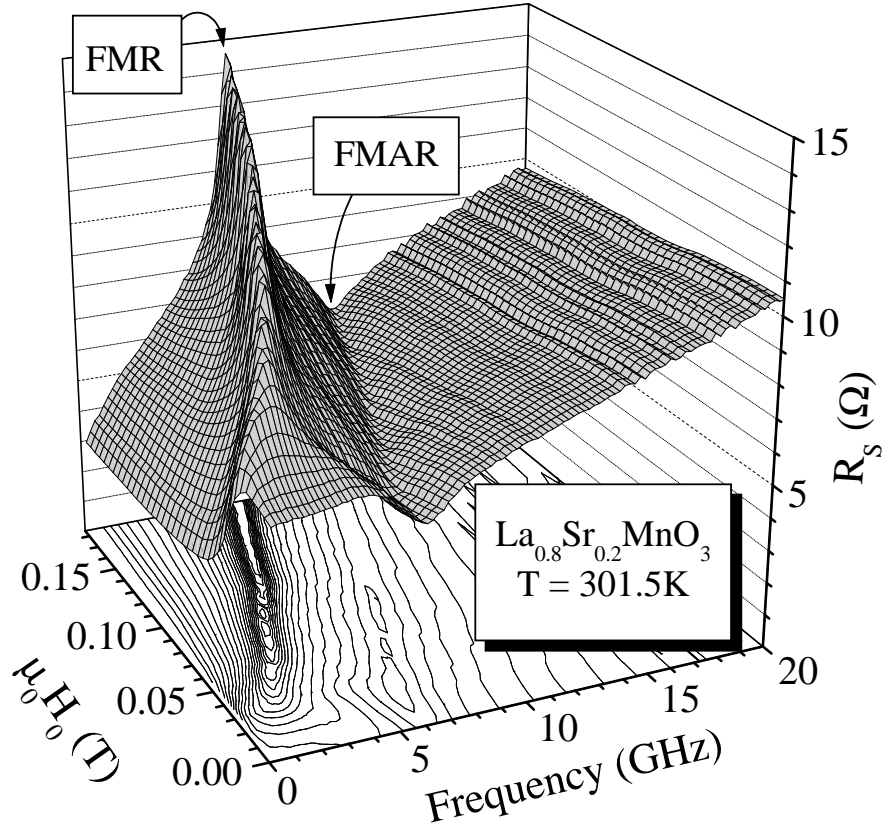
² S. Jin, T.H. Tiefel, M. McCormack, R.A. Fastnacht, R. Ramesh, and L.H. Chen, Science **264**, 413 (1994).

³ A.P. Ramirez, J. Phys.:Condens. Matter **9**, 8171 (1997), and references therein.

⁴ A. Urushibara, Y. Moritomo, T. Arima, A. Asamitsu, G. Kido, and Y. Tokura, Phys. Rev. B **51**, 14103 (1995).

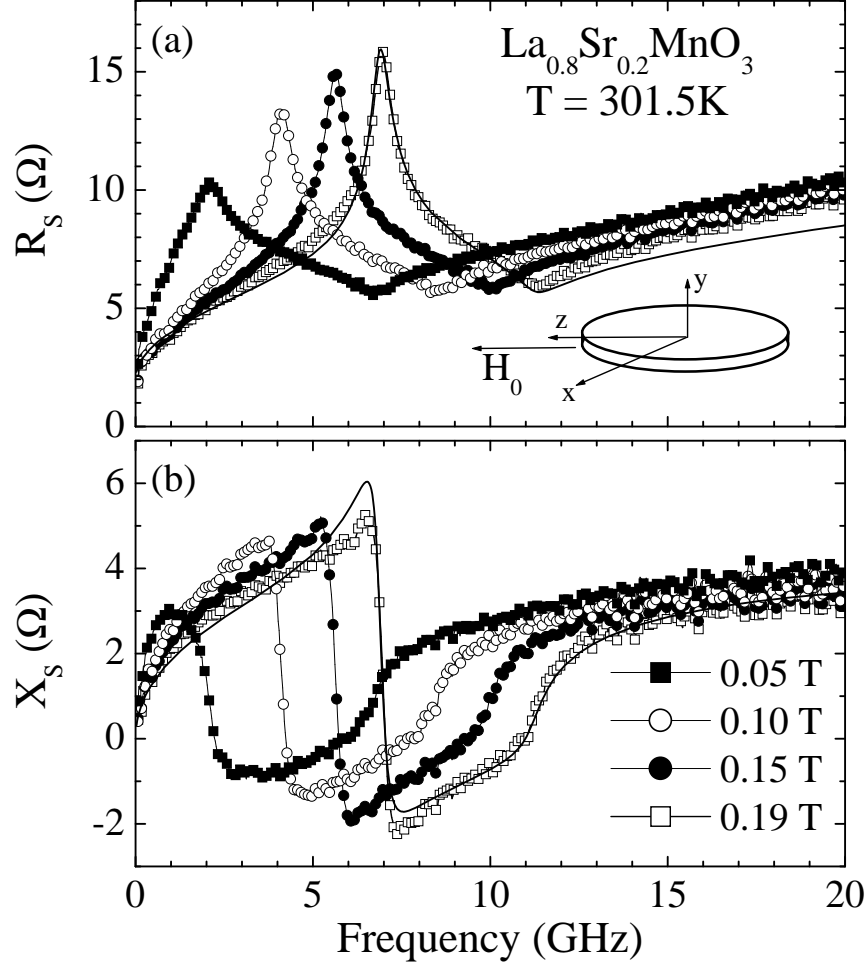
⁵ R. Mahendiran, S.K. Tiwary, A.K. Raychaudhuri, T.V. Ramakrishnan, R. Mahesh, N. Rangavittal, and C.N.R. Rao, Phys. Rev. B **53**, 3348 (1996).

- ⁶ K.H. Kim, J.H. Jung, and T.W. Noh, Phys. Rev. Lett. **81**, 1517 (1998).
- ⁷ M. Quijada, J. Cerne, J.R. Simpson, H.D. Drew, K.H. Ahn, A.J. Millis, R. Shreekala, R. Ramesh, M. Rajeswari, and T. Venkatesan, Phys. Rev. B **58**, 16093 (1998).
- ⁸ A.V. Boris, N.N. Kovaleva, A.V. Bazhenov, P.J.M. van Bentum, Th. Rasing, S-W. Cheong, A.V. Samoilov, and N-C. Yeh, Phys. Rev. B **59**, R697 (1999).
- ⁹ S.E. Lofland, S.M. Bhagat, S.D. Tyagi, Y.M. Mukovskii, S.G. Karagashev, and A.M. Balbashov, J. Appl. Phys. **80**, 3592 (1996).
- ¹⁰ S.E. Lofland, V. Ray, P.H. Kim, S.M. Bhagat, M.A. Manheimer, and S.D. Tyagi, Phys. Rev. B **55**, 2749 (1997).
- ¹¹ S.E. Lofland, S.M. Bhagat, K. Ghosh, R.L. Greene, S.G. Karabashev, D.A. Shulyatev, A.A. Arsenov, and Y. Mukovskii, Phys. Rev. B **56**, 13705 (1997).
- ¹² S.E. Lofland, P.H. Kim, P. Dahiroc, S.M. Bhagat, S.D. Tyagi, C. Kwon, R. Shreekala, R. Ramesh, and T. Venkatesan, J. Phys.: Condens. Matter **9**, 6697 (1997).
- ¹³ C.A. Ramos, M.T. Causa, M. Tovar, X. Obradors, and S. Pinol, J. Mag. Mag. Mat. **177–81**, 867 (1998).
- ¹⁴ Andrew Schwartz, Marc Scheffler, and Steven M. Anlage, Phys. Rev. B **61**, R870 (2000).
- ¹⁵ J.C. Booth, Dong Ho Wu, and Steven M. Anlage, Rev. Sci. Instrum. **65**, 2082 (1994).
- ¹⁶ The low resistivity of Cu, and it's small temperature dependence over the temperatures of interest in this study, make this an extremely good assumption.
- ¹⁷ B. Lax and K.J. Button, *Microwave Ferrites and Ferrimagnetics* (McGraw-Hill, New York, 1962).
- ¹⁸ Marc Scheffler, M.S. thesis, University of Maryland, 1998.
- ¹⁹ A.M. Balbashov, S.G. Karabashev, Ya.M. Mukovskiy, and S.A. Zverkov, J. Cryst. Growth **167**, 365 (1996).
- ²⁰ In the coaxial geometry, the microwave magnetic field lines are circular, and therefore h_{rf} is not everywhere orthogonal to H_0 , as was assumed by the model presented in Sec. III. In order to account for this we have calculated the effective impedance of the sample by assuming that the susceptibility varies as $\cos^2 \theta$ and performing the angular integration. In addition, we find that there is a small impedance mismatch between the coaxial cable and the sample which we have modeled as a parallel resistance and capacitance, and included in the effective impedance. It is this effective impedance which is fit to the data in Fig. 2.



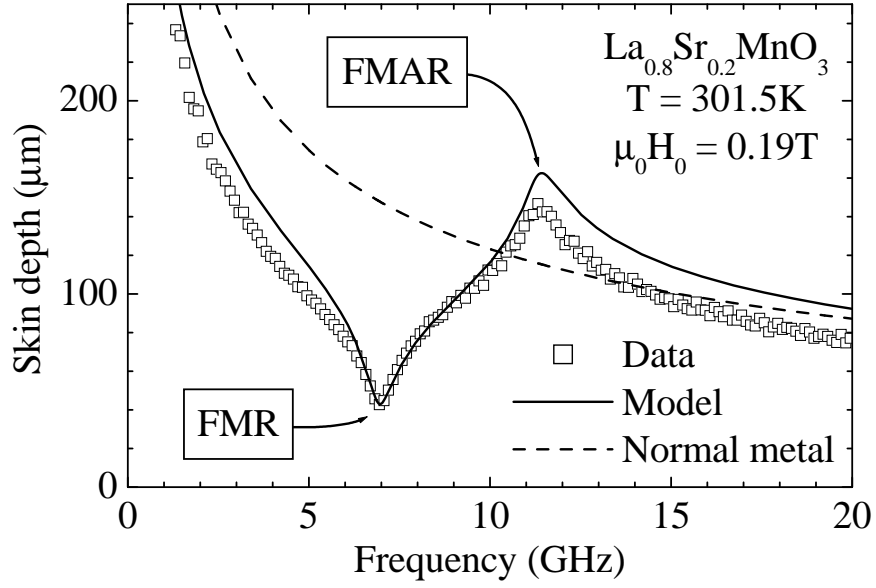
Schwartz *et al.*
Figure 1

FIG. 1. The frequency and field dependence of the surface resistance R_s of $\text{La}_{0.8}\text{Sr}_{0.2}\text{MnO}_3$ at $T = 301.5\text{ K}$. As indicated, the ferromagnetic resonance (FMR) and ferromagnetic anti-resonance (FMAR) are clearly visible. The frequency and field dependencies of these two features are seen in the contour plot projection onto the $f - H$ plane.



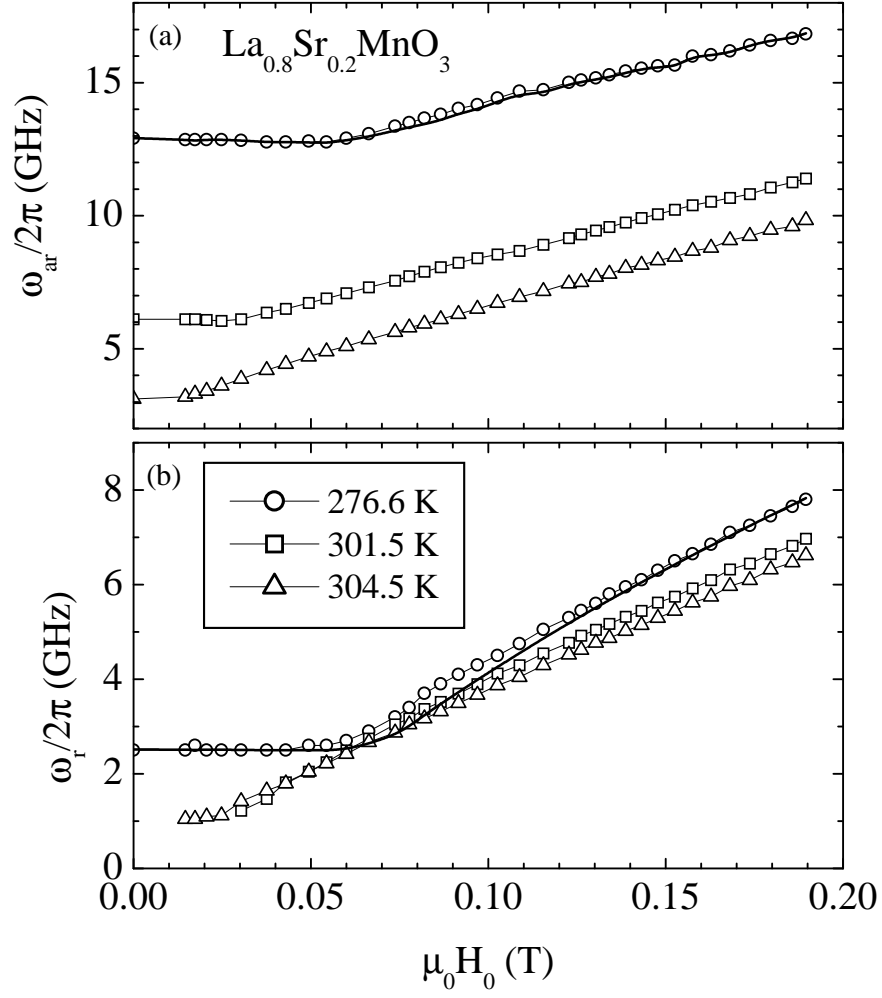
Schwartz *et al.*
Figure 2

FIG. 2. The frequency dependence of the 301.5 K surface impedance of $\text{La}_{0.8}\text{Sr}_{0.2}\text{MnO}_3$ at finite applied field. The orientation of the applied field H_0 and the axes relative to the disk-shaped sample is shown schematically. (a) Fixed-field cuts through the data displayed in Fig. 1, showing the frequency dependence of R_s for four different values of the applied field. (b) The corresponding surface reactance data at the same temperature and field values. The movement of both the FMR and FMAR features to higher frequency with increasing field is clearly seen in both sets of data. The thick solid line on both parts shows a fit of the model presented in Sec. III to the $\mu_0 H_0 = 0.19\text{ T}$ data.



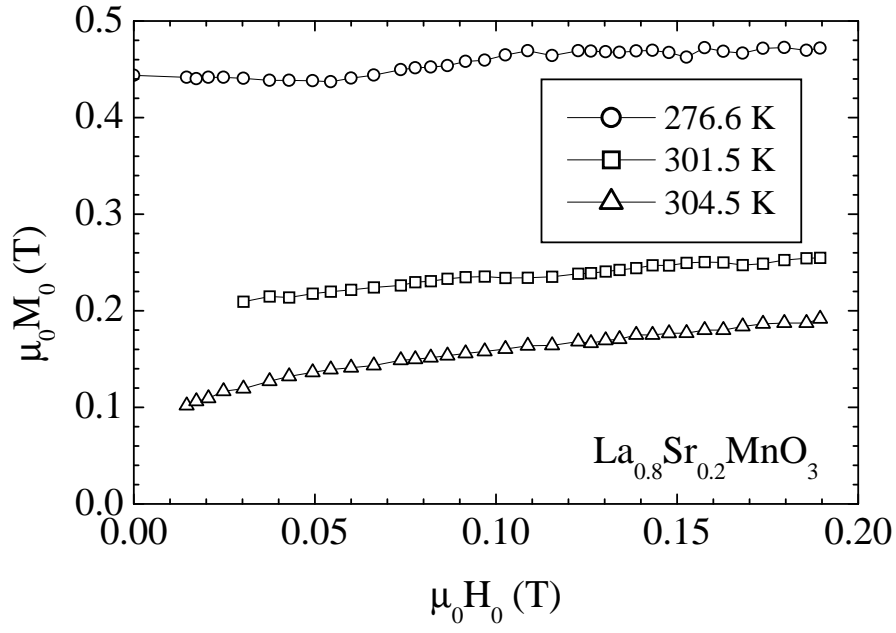
Schwartz *et al.*
Figure 3

FIG. 3. Frequency dependence of the skin depth $\delta = (\text{Re}\{\hat{k}\})^{-1}$ of $\text{La}_{0.8}\text{Sr}_{0.2}\text{MnO}_3$ at 301.5 K and 0.19 T. The open squares show the inverse of the real part of the wavevector, calculated from the 0.19 T data shown in Fig. 2 using Eq. (15). The solid line is extracted from the model presented in Sec. III, with the same parameters used in Fig. 2. The dashed line is the skin depth for a normal, non-magnetic metal with the same resistivity value, 60 mΩ-cm.



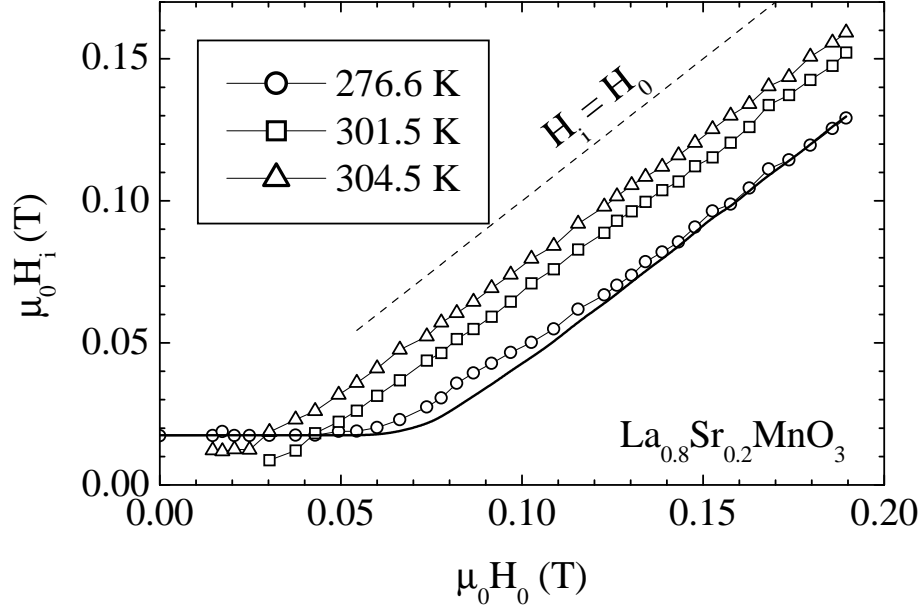
Schwartz *et al.*
Figure 4

FIG. 4. Field dependence of (a) the ferromagnetic anti-resonance frequency and (b) the ferromagnetic resonance frequency of $\text{La}_{0.8}\text{Sr}_{0.2}\text{MnO}_3$ at three representative temperatures. The thick solid lines are the empirical model discussed in Sec. IV B applied to the 276.6 K data.



Schwartz *et al.*
Figure 5

FIG. 5. The field dependence of the magnetization of $\text{La}_{0.8}\text{Sr}_{0.2}\text{MnO}_3$ at three representative temperatures, as calculated from the data in Fig. 4 using Eq. (13).



Schwartz *et al.*
Figure 6

FIG. 6. The field dependence of the internal field H_i at three representative temperatures, as calculated from the data in Fig. 4 using Eq. (16). The thick solid line is the empirical model discussed in Sec. IV B applied to the 276.6 K data. The dashed line represents $H_i = H_0$, and it is clear that all curves approach this slope for large values of H_0 .